Chapter 3

Recent Advances in $BiVO_4$- and Bi_2Te_3-Based Materials for High Efficiency-Energy Applications

Phuoc Huu Le, Nguyen Trung Kien and Chien Nguyen Van

Additional information is available at the end of the chapter

http://dx.doi.org/10.5772/intechopen.75613

Abstract

This chapter provides recent progress in developments of $BiVO_4$- and Bi_2Te_3-based materials for high efficiency photoelectrodes and thermoelectric applications. The self-assembling nanostructured $BiVO_4$-based materials and their heterostructures (e.g., WO_3/$BiVO_4$) are developed and studied toward high efficiency photoelectrochemical (PEC) water splitting via engineering the crystal and band structures and charge transfer processes across the heteroconjunctions. In addition, crystal and electronic structures, optical properties, and strategies to enhance photoelectrochemical properties of $BiVO_4$ are presented. The nanocrystalline, nanostructured Bi_2Te_3-based thin films with controlled structure, and morphology for enhanced thermoelectric properties are also reported and discussed in details. We demonstrate that $BiVO_4$-based materials and Bi_2Te_3-based thin films play significant roles for the developing renewable energy.

Keywords: $BiVO_4$, bismuth telluride (Bi_2Te_3), photoelectrochemical (PEC) water splitting, thermoelectrics, pulsed laser deposition

1. Bismuth vanadate ($BiVO_4$) material: a highly promising photoanode for use in solar water oxidation

The photoelectrochemical (PEC) water splitting, which uses semiconductors to directly harvest and convert the abundant solar energy into storable and friendly environmental energy in the form of hydrogen and oxygen from water, has been regarded as a promising approach to solve our current energy challenges [1–6]. The PEC cell for energy conversion on a global scale requires the development of devices that are highly efficient, stable, and simple in design. The effective

and economic energy transfer technologies are still under developing stage for more than 40 years. The PEC water splitting becomes more competitive as the cost continues to decrease with the development of nanotechnology, which offers the use of new nano-heterostructure photocatalysts. The current direction along this research field focuses on the development of high efficiency photoelectrodes based on metal oxides due to their high chemical and photostability, low cost, and ease of fabrication. Among these interesting and important photoelectrode materials for PEC, $BiVO_4$ is demonstrated as a promising photocatalyst for PEC water splitting. Originally, the $BiVO_4$ was intensively studied as a ferroelasticity, acoustic-optical, and ionic conductivity materials [7]; however, recently most studies focus on its photocatalytic activity owing to its direct bandgap of ~2.5 eV together with the desirable band edges and good stability [8–11]. Additionally, the theoretical solar-to-hydrogen conversion efficiency of the monoclinic $BiVO_4$ could reach 9.2% with a maximum photocurrent of 7.5 mA cm^{-2} under standard AM 1.5 solar light irradiation, which is significantly higher than those of the common metal oxides, and thus the monoclinic $BiVO_4$ has been recognized as one of the most promising photoanode materials for PEC water splitting [1]. However, its photoactivity performance is limited by its poor electrical conductivity, slow hole transfer kinetics for water oxidation, and poor charge separation [12]. A concise overview of $BiVO_4$ electronic and optical properties as well as the alternative strategies to improve its photocatalytic activities is discussed in this section.

2. Crystal and electronic structures of bismuth vanadate

The synthesis $BiVO_4$ crystallizes in three main crystal structures of tetragonal scheelite, monoclinic phase, and tetragonal zircon structure. The photocatalytic activities of $BiVO_4$ strongly depend on the optical properties of each crystal structure. Among these structures, the monoclinic scheelite $BiVO_4$ was demonstrated to exhibit the highest photocatalytic water oxidation under visible light illumination [13]. The higher photocatalytic activity of the monoclinic scheelite was attributed to its smaller energy band gap and higher crystal distortion, which enhance the optical absorption and the electron-hole separation [14]. The conduction-band minimum of $BiVO_4$ is formed mainly by V 3d, which splits into triplet bands V 3d $x^2–y^2/z^2$, V 3d z^2/zx, and V 3d zy/xy [15]. The valence band (VB) of tetragonal zircon structure $BiVO_4$ is formed by O 2p orbital, but the top region of VB of monoclinic structure is formed by both Bi 6 s and O 2p orbitals. It was demonstrated that Bi 6 s is located above O 2p and the smaller bandgap of monoclinic $BiVO_4$ attributes to the transition from the 6 s electrons of Bi to the 3d orbital of V [14, 16]. Recently, Zou et al. demonstrated that the crystal distortion in monoclinic $BiVO_4$ improves the lone-pair impact of Bi 6 s states which raises up the O 2p states and reduces the bandgap [17]. In addition, the monoclinic scheelite structure possesses the better electron-hole separation owing to its higher degree of structural distortion than that in the tetragonal scheelite structure to result in enhanced photocatalytic activity for the monoclinic structure. In addition, the conduction-band edge of $BiVO_4$ is only slightly below the H+/H2 redox potential, while its valence band is much below the oxidation potential of water resulting in low required external bias [15].

In order to investigate the experimental crystal and electronic structure of monoclinic $BiVO_4$, the single crystal $BiVO_4$, which possesses good crystallinity and eliminates the structural and electronic defects as well as impurity phases, is required. The vacuum deposition such as

http://dx.doi.org/10.5772/intechopen.75613

sputtering, molecular beam epitaxy, and pulsed laser deposition for the single crystal monoclinic $BiVO_4$ has been developed recently [18–20]. A good lattice match (mismatch less than 1%) of cubic yttrium-stabilized zirconia (YSZ, a = 5.145 Å) was used as substrate for epitaxial growth of high-quality epitaxial monoclinic $BiVO_4$ (a = 5.1935 Å, b = 5.0898 Å, c = 11.6972, γ = 90.3871) films. The X-ray diffraction θ–2θ scan (**Figure 1a**) shows only high intensity and sharp (00 l) reflections of monoclinic $BiVO_4$ phase indicating that growth was *c*-axis oriented: $BiVO_4$ (001) || YSZ (001). The high-resolution TEM image (the inset of **Figure 1**) reveals the

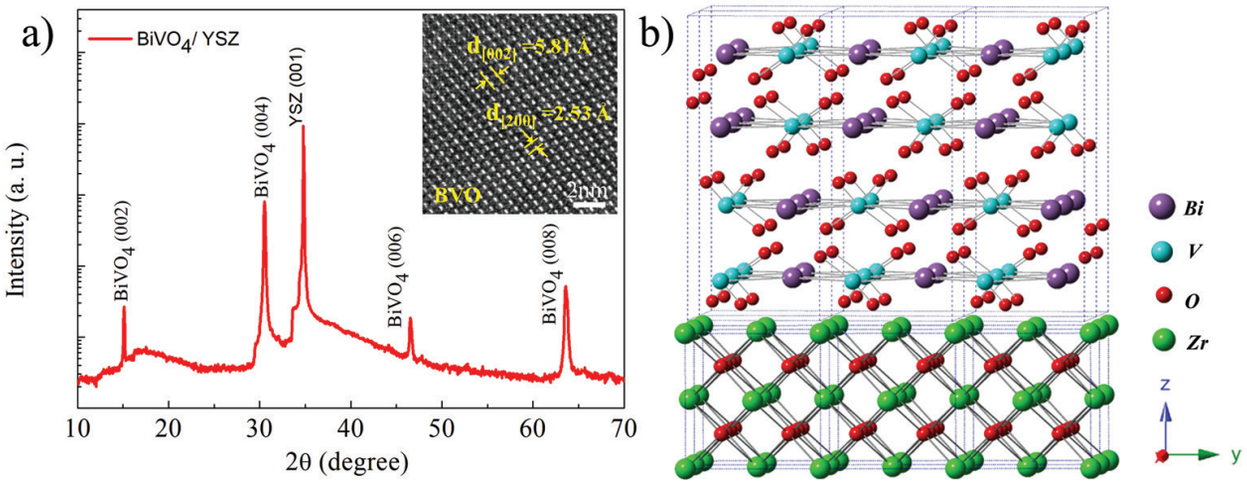

Figure 1. (a) XRD 2θ/θ scans of $BiVO_4$ film grown on YSZ substrate, and the inset shows HR-TEM image of $BiVO_4$; (b) atomic model of $BiVO_4$/ YSZ heteroconjunction.

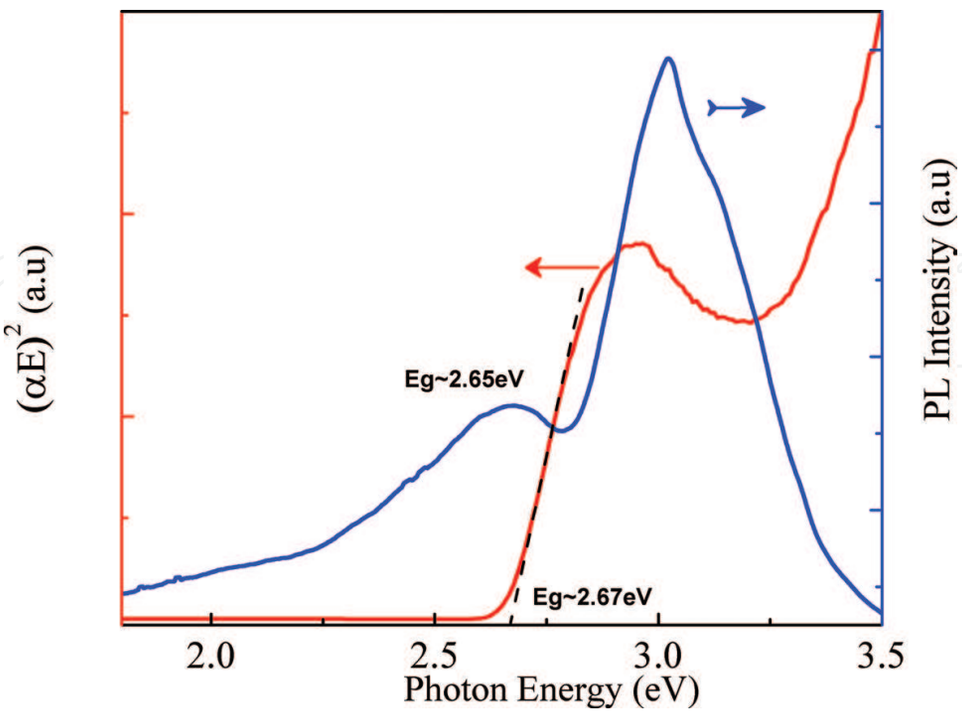

Figure 2. Photoluminescence taken under the irradiation of 325 nm laser at room temperature (green curve) and UV-Vis absorption spectrum (red curve) of $BiVO_4$ epitaxial film.

in-plane and out-of-plane lattice parameters of the $BiVO_4$ with d_{200} = 2.53 Å and d_{002} = 5.81 Å which are in good agreement with the lattice constants of the bulk monoclinic $BiVO_4$. The orientation and growth direction of $BiVO_4$ crystal were identified and constructed in the corresponding atomic model as shown in **Figure 1b**.

The electronic structural properties of single crystal $BiVO_4$ were investigated by the photoluminescence (PL) spectroscopy and UV-Visible spectroscopy. **Figure 2** presents the PL and UV-Vis absorption spectra of a single crystal $BiVO_4$ film. As presented in the UV-Vis absorption spectrum, the observed absorption in the range of 440–480 nm corresponding to the bandgap of ~ 2.67 eV could attribute to the transition from the 6 s electrons of Bi (or the hybrid orbital of Bi 6 s and O 2p) to the empty 3d x^2-y^2/z^2 orbital of V, which is consistent with emission peak of 2.65 eV in the PL spectrum. The second absorption band edge of approximately 3.15 eV and the second PL emission peak at 3.1 eV could be ascribed to the electron transition from O 2p valence band to V 3d z^2/zx and/ or V 3d zy/xy orbitals.

3. Strategies to enhance photoelectrochemical properties of $BiVO_4$

The development of suitable techniques to fabricate high efficiency $BiVO_4$ photoelectrode for PEC water spitting is crucial. To date, there are many methods, which have been developed to prepare $BiVO_4$ photoelectrodes for use in solar water oxidation. The representative synthesis methods are (1) metal organic decomposition (MOD) combining with the spin coating or spray pyrolysis deposition [21–23], (2) electrophoretic deposition (EPD) and chemical bath deposition (CBD) [24–27], and (3) vacuum deposition methods such as sputtering deposition and pulsed laser deposition (PLD) [18–20, 28–29]. The MOD is a facile method to synthesize $BiVO_4$ materials for photoelectrodes. The main advantages of the MOD method are the easy composition tuning and morphology engineering. However, the existence of crystal and surface defect and low adhesion between $BiVO_4$ and conducting substrate could limit its performance. The EPD and CBD methods are simple, have low cost, and are easy to scale up. The vacuum deposition is a powerful method to synthesize good crystalline $BiVO_4$ photoelectrodes. The samples prepared by this method could easily control the doped composition; could facilely tune the crystalline in form of amorphous, polycrystalline, and single crystalline; and possess a good adhesion.

As described above, $BiVO_4$ has many advantages features, however, the actual PEC performance of undoped $BiVO_4$ is still far below its theoretical value, indicating that its advantages have not been fully developed. Many research groups have improved photoelectrochemical water oxidation by the introduction of (1) controlled morphologies, (2) forming nanocomposite structure, (3) doping, and (4) decorating with cocatalysts [30]. A summary of advantages and alternative strategies to enhance photoelectrochemical properties of $BiVO_4$ was depicted in **Figure 3**. The best PEC performance of $BiVO_4$ photoelectrodes that has been demonstrated to date is a combination of several above strategies to take advantages of high surface area, high electron mobility, high water oxidation kinetics, and low charge carrier recombination. Therefore, understanding the benefits and disadvantages of each strategy could provide an effective way to enhance the PEC properties.

http://dx.doi.org/10.5772/intechopen.75613

First, the morphologies of $BiVO_4$ photoelectrode such as shape, size, and particle contact strongly effect on their interfacial energetics, kinetics, and charge transport properties as well as reactive sites. Because the electrochemical reactions only occur at the electrode-electrolyte interfacial area, the photogenerated electron-hole needs to be transferred to the surface for the reactions. Thus, the development of high surface area photoelectrodes is necessary. The porous structure and one-dimensional nanostructure such as nanorod/nanowire arrays reveal high surface areas per electrode volume, which directly improves the PEC efficiency. The high efficient PEC devices based on the $BiVO_4$ porous structure and the one-dimensional nanostructures have been reported by many research groups [31–34]. However, creating more porosity or smaller nanorod/nanowire structures to improve surface area could increase the defect site, increase grain boundaries, and reduce crystallinity leading reduction photocatalytic activity [35]. In addition, with hole diffusion length of ~100 nm and carrier mobility of 0.044 $cm^2\ V^{-2}\ s^{-1}$ [36], the length and thickness of nanostructure should be finely optimized to maximum light absorption and photogenerated charge carrier transport. Furthermore, researchers have recently demonstrated that the charge separation and photoactivity properties are closely related to the exposed crystal facet of $BiVO_4$ photocatalysts [8–9, 37–39]. Therefore, an optimized design and morphological control of crystal facets could improve the PEC performance.

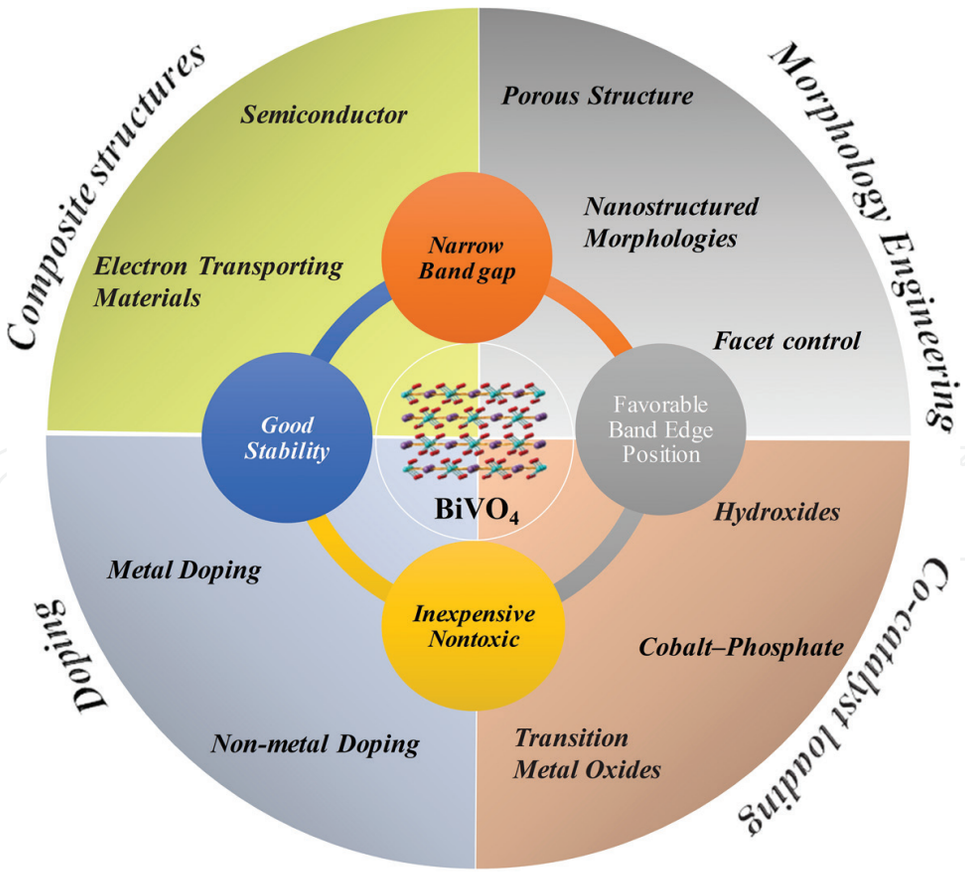

Figure 3. The advantages and strategies to enhance photoelectrochemical properties of $BiVO_4$.

Second, nanocomposites provide a powerful route to overcome limitations in the current studies of single material systems for water splitting, where the photoelectrochemical performance of photoelectrode can be significantly improved by the choice of proper interactions of constituents. The construction of nanocomposite consisting of $BiVO_4$ and addition semiconductor/or conductor can improve the optical absorption, charge carrier separation, and charge transport processes. Combination of $BiVO_4$ with additional metal oxide semiconductors could enhance overall photon absorption and improve electron-hole separation by the rapid photogenerated electron and hole injections at their heterojunctions and extension the optical absorption range. Many $BiVO_4$-based heterostructures have been fabricated successfully such as $TiO_2/BiVO_4$, $Ag_3PO_4/BiVO_4$, $Bi_2S_3/BiVO_4$, g-C3N4/$BiVO_4$, $BiVO_4/SnO_2$, $WO_3/BiVO_4$, BiOCl/$BiVO_4$, $Fe_2O_3/BiVO_4$, $Cu_2O/BiVO_4$, and ZnO/$BiVO_4$ [40–43]. Among them, the WO_3 is a commonly coupled semiconductor with $BiVO_4$ because it is a stable n-type semiconductor with better electron transport properties than the $BiVO_4$ and a suitable conduction-band edge for facile electron injection from conduction band of $BiVO_4$ [29, 44–46].

Recently, we reported a self-assembled nanocomposite photoanode composed of epitaxial $BiVO_4$ matrix embedded with WO_3 mesocrystal for photoelectrochemical application in the visible light regime using PLD [29]. By taking the advantage of the structural feature of this heterostructure, the well-defined crystal facet and interface between WO_3 and $BiVO_4$ phases provide a template for the fundamental understanding of photoactivity in the nanocomposite. The $BiVO_4$-WO_3 crystal structure details were investigated by XRD and TEM as shown in **Figure 4**. The XRD 2θ-θ scans, in-plane Φ-scans, and reciprocal space map results clearly show that $BiVO_4$ and WO_3 spontaneously separated into two single phases during the deposition with an in-plane orientation relationship as $[100]_{BiVO4}$ //$[110]_{WO3}$ //$[001]_{YSZ}$. Both monoclinic $BiVO_4$ and orthorhombic WO_3 phases exhibit two sets of structural domains, which are separated by a 90° rotation around *c*-axis. The microstructure and the epitaxial relationship of $BiVO_4$-WO_3 heterostructure were further investigated as displayed in **Figure 4(b–e)**, which are in an excellent agreement with the XRD analyses. The self-assembled mesocrystal-embedded heterostructure that composed WO_3 and $BiVO_4$ phases is illustrated in **Figure 4g**. The energy band alignment of $BiVO_4$-WO_3 heterojunction illustrated using X-ray photoelectron spectroscopy technique shows that the valence band maxima of WO_3 lies 0.55 eV below that of $BiVO_4$ and the conduction-band minimum of WO_3 lies 0.25 eV below that of $BiVO_4$. This energy band structure could favor the enhancement of photogenerated charge carrier separation, which was further confirmed by photoluminescence and ultrafast transient absorption spectroscopies. **Figure 5** shows Nyquist electrochemical impedance spectroscopy and Mott-Schottky analysis for the $BiVO_4$-WO_3 photoelectrodes. The results demonstrated a much higher electron conductivity of WO_3 with carrier densities of 9.68×10^{18} cm^{-3} under light illumination than $BiVO_4$. Therefore, the $BiVO_4$ matrix serves as the light absorber due to its narrow band-gap, and the WO_3 mesocrystal acts as an electron conductor owing to its high electron conductivity resulting in a significantly enhanced photoelectrochemical performance.

Further example could be observed in the double-deck inverse opal $WO_3/BiVO_4$ structure that could reach a photocurrent density of 3.3 mA/cm^2 at 1.23 V versus RHE and the core-shell $WO_3/BiVO_4$ helix nanostructure, in which $BiVO_4$ was doped with Mo and naturally doped with W from the WO_3 core, exhibits a high photocurrent density of 3.6 mA/cm^2 at 1.23 V versus RHE [34, 47]. More recently, the highest photocurrent density of 6.72 mA/cm^2 at 1.23 V versus RHE for

http://dx.doi.org/10.5772/intechopen.75613

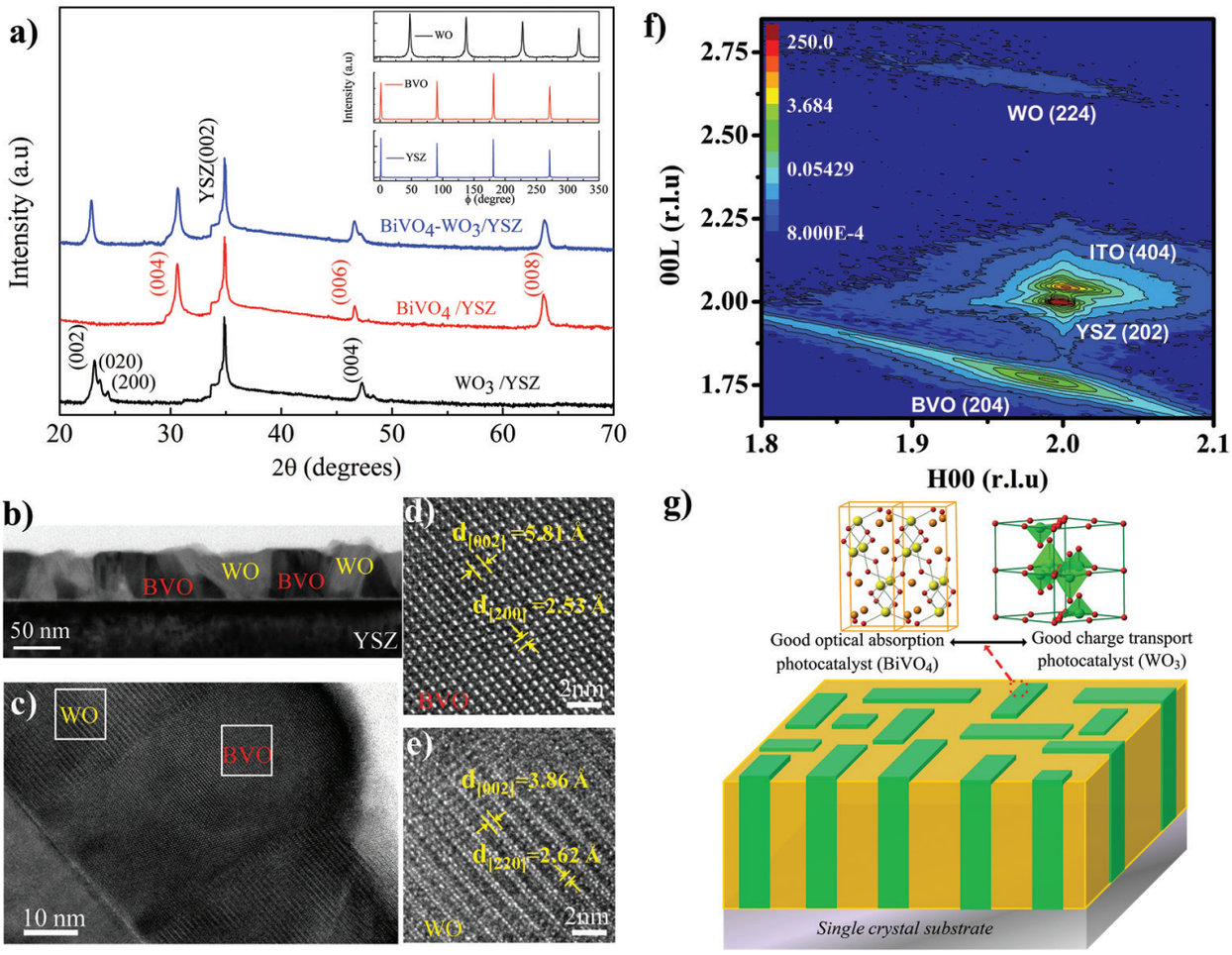

Figure 4. Structure characterization of $BiVO_4$-WO_3 nanocomposite. (a) X-ray diffraction 2θ-θ scans of pure WO_3, $BiVO_4$, and the $BiVO_4$-WO_3 nanocomposite showing only (00 *l*) type peaks of $BiVO_4$ and WO_3. Inset shows XRD φ-scans of YSZ (220), $BiVO_4$ {013}, and WO_3 {022} reflections for $BiVO_4$-WO_3 heterostructure. (b-e) Cross-sectional TEM images of $BiVO_4$-WO_3 (BVO-WO) nanocomposite taken along $[010]_{YSZ}$ zone axis. The enlarged images taken from the marked areas of (d) $BiVO_4$ and (e) WO_3 showing their out-of-plane and in-plane d-spacing parameters. (f) X-ray reciprocal space maps (RSMs) of the composite grown on ITO/YSZ. (g) Illustration of self-assembled $BiVO_4$-WO_3 nanocomposite [29].

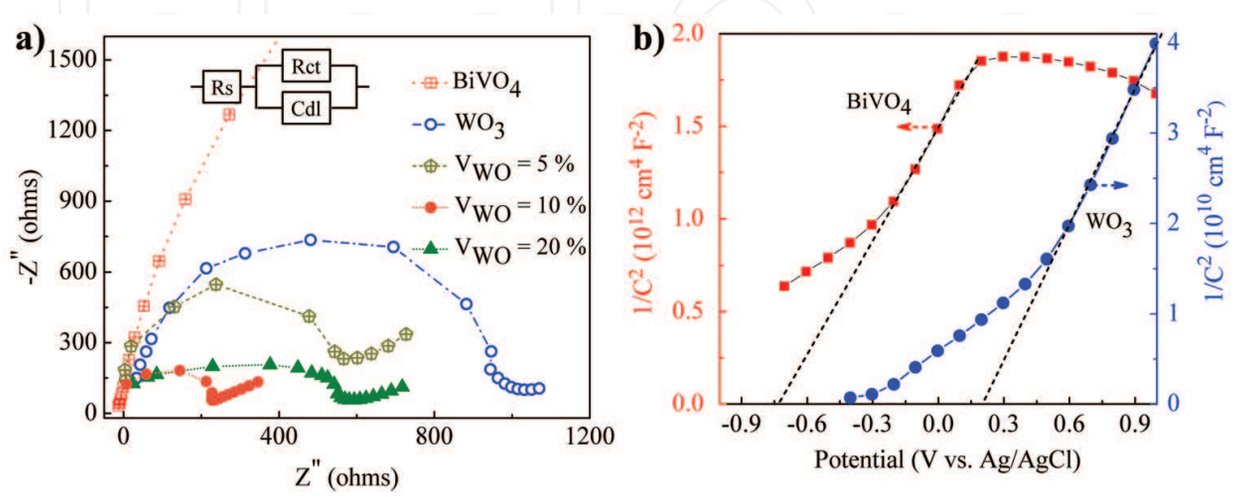

Figure 5. (a) The Nyquist plots and (b) the Mott-Schottky plots for the WO_3, $BiVO_4$, and $BiVO_4$-WO_3 photoelectrodes in 0.5 M Na_2SO_4 solution under AM 1.5 illumination [29].

$BiVO_4$-based photoelectrode was obtained in the CoPi-coated $WO_3/BiVO_4$ core-shell nanorods [21]. The high efficiency photoelectrode was attributed to the superior charge carrier separation and efficient light scattering. In addition, by coupling with a conductor such as reduced graphene oxide and carbon nanotubes, the photocurrent density of the composite electrodes was improved significantly compared to those of the corresponding $BiVO_4$ electrodes which could attribute to the enhancement of charge separation and transport properties [49–57]. However, due to the low crystallinity of $BiVO_4$ as well as the poor $BiVO_4$-conductor and conductor-substrate contact in these nanocomposites, it needs to be further developed to improve the PEC performance.

Third, doping with the metal (such as W, Fe, B, Cu, Zn, Ti, Nb, Sn, Co, Pd, Rb, Ru, Ag, Ga, Sr, and Ir) or nonmetal (such as P and N) materials can change the electrical and optical properties of $BiVO_4$. Among them, only Mo- and W-doped $BiVO_4$ show a significantly enhanced photocurrent and IPCE [21]. The intentional introduction of n-type conductivity W and/or Mo atoms does not change the bandgap energy and band edge positions of doped-$BiVO_4$; however, it can increase the charge carrier density and the electrical conductivity. A suitable doping concentration of Mo and/or W results in significant improvement PEC performance of $BiVO_4$ [54–56]. On the other hand, P doping forms an internal electric field which may improve the photogenerated electron–hole separation. However, it is noted that the doping could induce trap carrier which can enhance charge carrier recombination and reduce the charge transport [35]. Therefore, the optimum doping concentration is a key factor to improve the overall PEC performance of the photoelectrode.

Finally, decoration of $BiVO_4$ with various oxygen evolution catalysts (OECs) such as Co–Pi, Co_3O_4, RhO_2, Pt, CoO, and FeOOH improves the kinetic for oxygen evolution and provides unique active sites for catalytic reactions, thereby strongly enhanced the photocurrent density [3, 27, 40, 57–58]. In addition, it decreases the bias potential and improves the stability of $BiVO_4$ photoanodes. Perhaps the most successful route in the development of high efficient $BiVO_4$ photoelectrode for water oxidation is the modification of the $BiVO_4$-semiconductor nanocomposite surface with OECs. To date, the highest photocurrent density 6.72 mA/cm^2 at 1.23 V versus RHE was obtained for the CoPi-coated $WO_3/BiVO_4$ core-shell nanorods [48].

4. Introduction to thermoelectric bismuth-based materials and applications

Thermoelectric (TE) materials are used in appliances such as heat pumps and power generators [59–63]. TE devices offer unique features of low environmental impact, no moving parts, quiet operation, and high reliability. The performance of TE materials is determined by a dimensionless figure of merit, $ZT = \alpha^2\sigma T/\kappa$, in which α, σ, T, and κ are the Seebeck coefficient, the electrical conductivity, absolute temperature, and the thermal conductivity, respectively. A TE material must exhibit a high power factor ($PF = \alpha^2\sigma$) and low thermal conductivity (κ) to achieve a high ZT value. However, it is challenging for enhancing the ZT value due to the coupling among the TE parameters [62]: the relationship between α and the carrier concentration n (expressed by $|\alpha| \sim n^{-2/3}$ approximately [60]) limits the increase of the PF ($=\alpha^2\sigma$), while the proportional relationship between electrical conductivity and electronic thermal conductivity (the Wiedemann-Franz law) restricts the enhancement of the σ/κ ratio.

Bismuth (Bi)-based chalcogenide narrow-bandgap semiconductors such as Bi_2Te_3, Bi_2Se_3, Sb_2Te_3, $Bi_2(Te_xSe_{1-x})_3$, and $(Bi_xSb_{1-x})_2Te_3$ are of high interest [64–69]. They have been widely exploited for Peltier coolers and thermoelectric generators at low temperature regime (≤150°C) [70, 71]. Thanks to the extensive phonon scattering at grain boundaries, nanocrystalline and nanostructured Bi-based chalcogenide thin films have achieved reduced thermal conductivity [72–77]. However, the lattice imperfections and grain-boundary defects impair the electrical transport properties of the films [72], which call for further investigations to improve PF or the electronic part of ZT. Currently, enhancing the PF of Bi-based thin films is challenging due to not only the coupling among TE material properties [60] but also the tendency of forming nonstoichiometric films at elevated substrate temperatures (T_s) [78]. Numerous charge carriers arising from vacancy defects of volatile elements can constrain the enhancement of $|\alpha|$; however, low carrier concentrations can suppress electrical conductivity if carrier mobility (μ) is poor.

The crystal structures of Bi_2Se_3 and Bi_2Te_3 are usually described by a hexagonal cell that consists of 15 layers of atoms stacking along the c-axis with a sequence shown below [60], as shown in **Figure 6**. ··· $Se^{(1)}$–Bi–$Se^{(2)}$–Bi–$Se^{(1)}$ ··· $Se^{(1)}$–Bi–$Se^{(2)}$–Bi–$Se^{(1)}$ ··· $Se^{(1)}$–Bi–$Se^{(2)}$–Bi–$Se^{(1)}$ ··· and ···$Te^{(1)}$–Bi–$Te^{(2)}$–Bi–$Te^{(1)}$ ··· $Te^{(1)}$–Bi–$Te^{(2)}$–Bi–$Te^{(1)}$···$Te^{(1)}$–Bi–$Te^{(2)}$–Bi–$Te^{(1)}$ ···. The superscripts refer to two different types of bonding for Se or Te atoms. The five-atomic-layer thick lamellae of –($Se^{(1)}$–Bi–$Se^{(2)}$–Bi–$Se^{(1)}$)– or –($Te^{(1)}$–Bi–$Te^{(2)}$–Bi–$Te^{(1)}$)– is called quintuple layers, QLs. The $Se^{(1)}$…$Se^{(1)}$ or $Te^{(1)}$…$Te^{(1)}$ refers to van der Waals force between Se and Te atoms, whereas the $Se^{(1)}$–Bi and Bi–$Se^{(2)}$ or $Te^{(1)}$–Bi and Bi–$Te^{(2)}$ are ionic-covalent bonds. This weak binding between the $Se^{(1)}$ – $Se^{(1)}$ and $Te^{(1)}$…$Te^{(1)}$ accounts for the easy cleavage of these materials perpendicular to the *c*-axis and the anisotropic thermal and electrical transport properties. For example, the thermal conductivity along the *c*-axis direction is ~0.7 $Wm^{-1}K^{-1}$, while it is ~1.5 $Wm^{-1}K^{-1}$ for the plane perpendicular to the *c*-axis [79].

Thin-film technology is advantageous for obtaining nanocrystalline and nanostructured materials by adjusting deposition conditions and subsequent thermal treatments. The extensive phonon scattering at grain boundaries in the nanostructures causes a large reduction in thermal conductivity while maintaining reasonable electrical conductivity, leading to enhanced ZT. Among physical vapor deposition techniques, PLD offers a great versatility in the fabrication of films with multielement stoichiometry and with a variety of structures, from amorphous or nanostructured to polycrystalline or even epitaxial [66–68, 76, 77, 80, 81]. Thin-film TE devices offer some distinctive advantages.

First, a thin-film device has the natural advantage of a small volume (thickness of ≤10 μm, length and width of ~100 μm) as compared to size of millimeters for a bulk TE couple. As a result, thin-film TE cooling can be integrated into microelectronic systems (**Figure 7a**). In principle, the bulk device can be scaled down to micro sizes; however, fabrication processes to do so are difficult.

Second, thin-film devices have a much shorter response time than bulk devices, as shown in **Figure 7c** [59]. The thin-film device achieves the steady state in 15 μs, while the bulk device requires 0.35 s [59]. This is a result of the response time associated with the transport of heat through the thin film (micrometers) rather than through the millimeters associated with bulk devices.

Third, the thin-film device has the ability to handle much larger density of heat pumping power than does the bulk device. Typically, bulk devices are working with pumping power

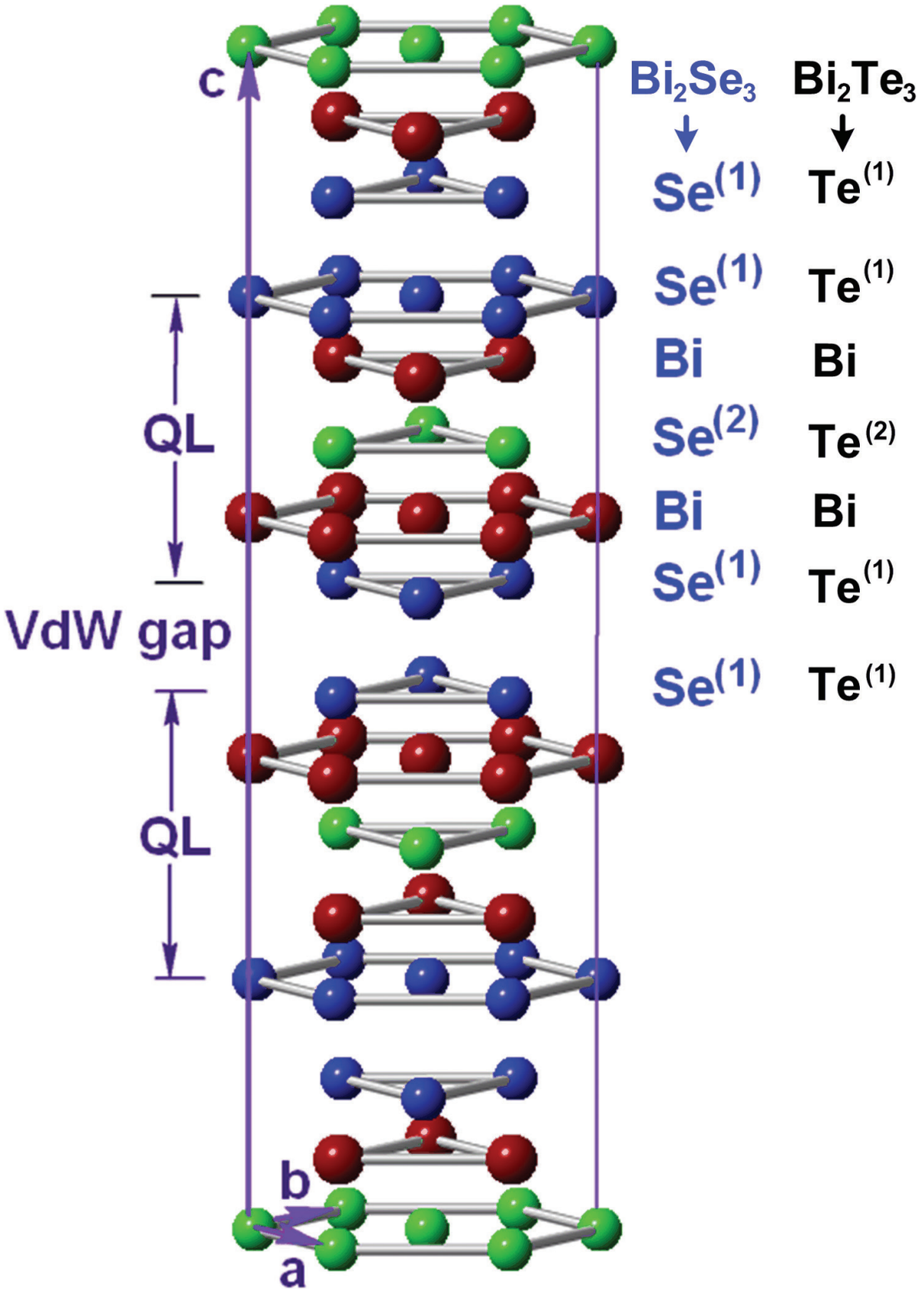

Figure 6. The hexagonal structures of one unit cell of Bi_2Se_3 and Bi_2Te_3.

http://dx.doi.org/10.5772/intechopen.75613

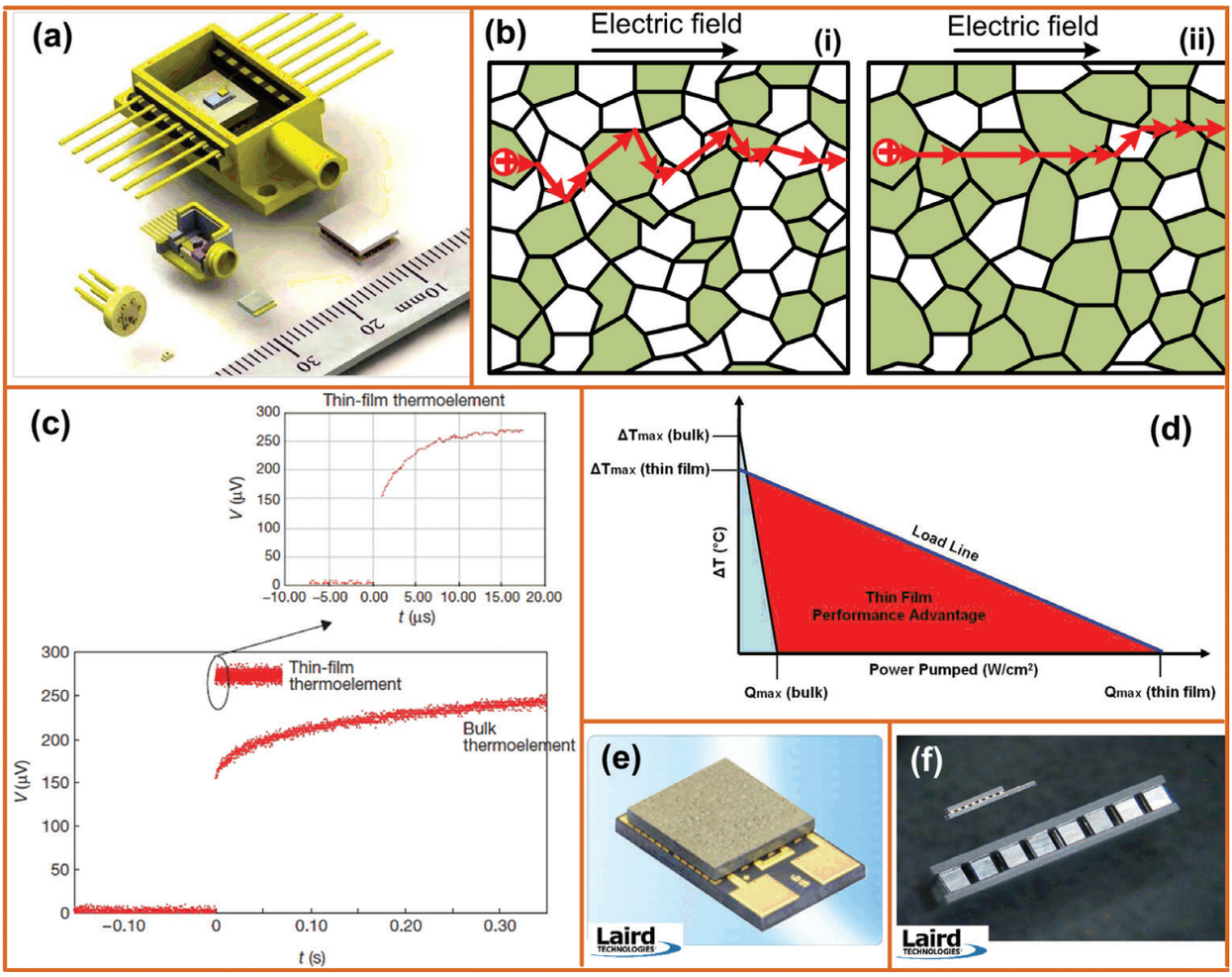

Figure 7. (a) An example for optoelectronics of the continuing reduction in package size. (b) A schematic of grain-boundary scattering for thin-film materials with (i) disoriented-small grains and (ii) highly oriented large grains. (c) The comparison of thermal/cooling time response of thin-film (~5 μm) superlattice device and a bulk device [59]. (d) Thermoelectric module performance chart which presents the temperature drop ΔT versus pumping power [83]. (e) A commercial thin-film TE module. (f) Size comparison between a thin-film TE device and bulk TE device [83].

density lower than 10 W/cm^2; however, the pumping power density in a thin-film device is on the order of hundreds of W/cm^2 [82]. **Figure 7d** illustrates a comparison performance chart between thin-film and bulk TE modules, in which the load line represents the temperature difference (ΔT) between the top and bottom substrate and possible pumping power density (Q) for a given drive current of a TE module [83]. At the maximum drive current for a TE module, the load line is determined by the maximum power density (Q_{max}) and the ΔT_{max}. For a commercial example, under a given drive current, an eTEC™ Series thin-film TE module (Laird technology) possesses a larger pumping power up to ten times (**Figure 7e**) and a comparable maximum temperature difference ΔT_{max} than the conventional bulk TE modules [83].

Fourth, the granular structure-morphology of thin films increases the grain-boundary scattering which is helpful for suppressing κ and enhanced ZT values. **Figure 7b** represents the roles of grain orientation and grain size in carrier mobility. The grains with the same colors illustrate that they have the same/similar orientations. The grain-boundary scattering in

Figure 7b(i) will be greater than that of the **Figure 7b(ii)** case because of its smaller grain size and the greater grain disorientation. The effective mobility is given by [84]

$$\mu_g = \frac{Lq}{\sqrt{2\pi m^* kT}} \exp\left(-\frac{\phi_b}{kT}\right) \quad (1)$$

where q is the carrier charge, m^* is the effective mass, k is the Boltzmann constant, T is the temperature, and ϕ_b is the grain-boundary potential barrier in the depletion region. In polycrystalline silicon, the potential barrier height is approximately twice as high at random boundaries as at low-energy coincidence boundaries.

5. Thermoelectric properties of nanocrystalline and nanostructured Bi_2Te_3-based thin films

Thermoelectric Bi_2Te_3-based materials have played a dominant role in the field of thermoelectrics. The traditional cooling materials are alloys of Bi_2Te_3 with Sb_2Te_3 (such as $Bi_{0.5}Sb_{1.5}Te_3$; p-type) and of Bi_2Te_3 with Bi_2Se_3 (such as $Bi_2Te_{2.7}Se_{0.3}$; n-type), with a ZT at room temperature approximately equal to one [63]. Recently, nanocrystalline and nanostructured Bi_2Te_3-based thin films have recently attracted great interests because of their superior TE performance [72–77, 80, 81, 85, 86]. The PF of Bi_2Te_3 films was 8.8 $\mu Wcm^{-1} K^{-2}$ for an (015)-oriented film with layered-hexagonal morphology [85] and 33.7 $\mu Wcm^{-1} K^{-2}$ for a highly (00l)-oriented layered film [86]. Furthermore, the hexagonal-Bi_2Te_3 film grown using MBE obtained a PF of 27 $\mu Wcm^{-1} K^{-2}$ [87], and the smooth-epitaxial- Bi_2Te_3 film prepared by co-evaporation achieved a PF of 39.9 $\mu Wcm^{-1} K^{-2}$ [88].

Despite fewer studies performed on thermoelectric Bi_2Se_3 as compared to Bi_2Te_3, a considerable amount of recent efforts to enhance TE performance has been devoted to the synthesis of Bi_2Se_3 nanostructures such as hexagonal flakes (PF ≈ 0.28 $\mu Wcm^{-1} K^{-2}$) [89] and nanoflakes (PF ≈ 0.97 $\mu Wcm^{-1} K^{-2}$) [90], using the solvo-thermal method and chemical bath deposition, respectively. Moreover, the Bi_2Se_3 film grown by metal organic-chemical vapor deposition has reached a PF = 5.8 $\mu Wcm^{-1} K^{-2}$ [91]. In PLD, tightly controlling substrate temperatures (T_s)

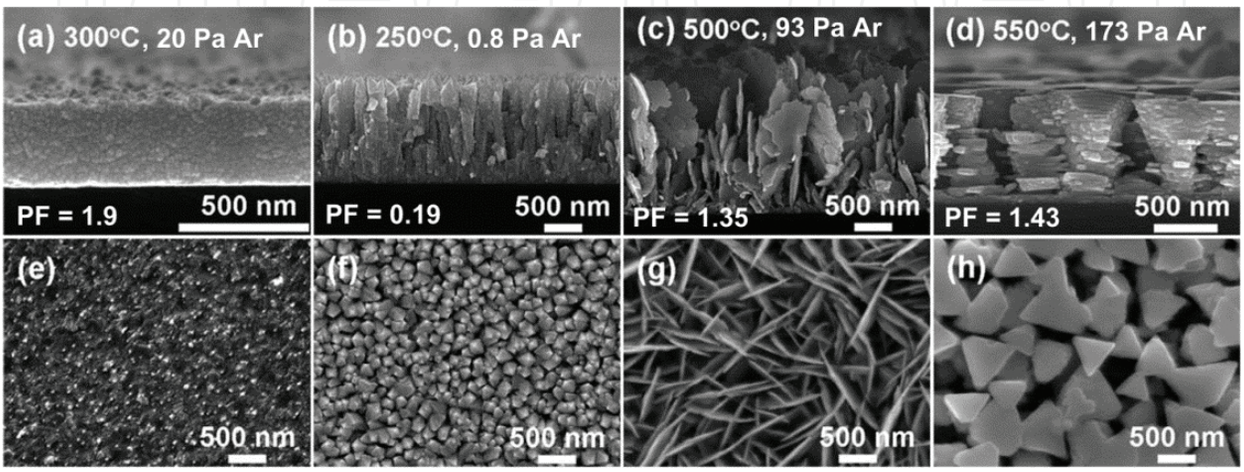

Figure 8. The morphology and power factor (PF, unit $\mu Wcm^{-1} K^{-2}$) of nanostructured Bi_2Te_3 thin films grown by PLD at various substrate temperatures and ambient pressures, reported by Chang and Chen [77].

http://dx.doi.org/10.5772/intechopen.75613

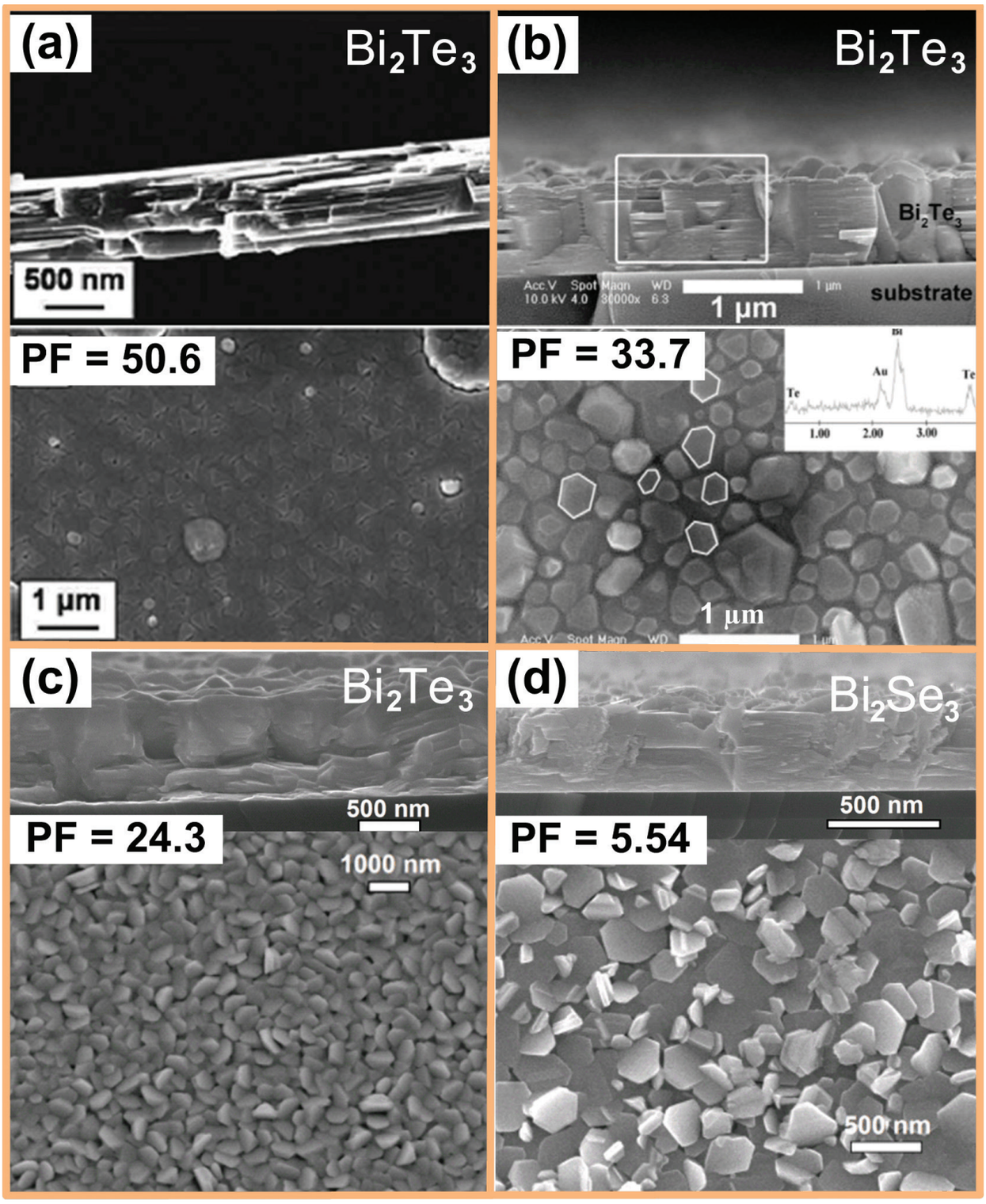

Figure 9. The morphology and power factor (PF, unit $\mu Wcm^{-1} K^{-2}$) of the optimal Bi_2Te_3 and Bi_2Se_3 thin films with layered structures grown by PLD, reported in Refs. [66, 67, 80, 86].

and ambient pressures enable the morphologies and compositions of films to be manipulated extensively, which offer a new method for enhancing the TE properties of films. For example, self-assembled Bi_2Te_3 films featuring well-aligned zero- to three-dimensional nanoblocks have been fabricated (**Figure 8**), but the room temperature PFs of these films remain low (≤ 1.9 $\mu Wcm^{-1} K^{-2}$) due to the low electrical conductivity of the voided structures [77].

By contrast, the Bi_2Te_3-based thin films with compact and/or layered structures possess the high electrical conductivities and relatively high Seebeck values if the films obtain stoichiometry. For example, A. Li Bassi et al. reported a high PF of 50.6 μWcm^{-1} K^{-2} for the layered-smooth Bi_2Te_3 films (**Figure 9a**) [80]. Similarly, the Bi_2Te_3 films with layered-hexagonal grain structure exhibited a high PF of 33.7 μWcm^{-1} K^{-2} (**Figure 9b**) [86]. P.H. Le et al. found that the optimal PF films also present compact-layered structures, namely, PF = 24.3 μWcm^{-1} K^{-2} for the Bi_2Te_3 film (**Figure 9c**) and PF = 5.54 μWcm^{-1} K^{-2} for the hexagonal Bi_2Se_3 film (**Figure 9d**) [66, 67]. Usually, compact or layered structure films obtain high carrier mobility than those with the open/voided nanostructures.

Table 1 summarizes thermal transport properties (at room temperature) of nanocrystalline-nanostructured Bi_2Te_3-based thin films and bulk materials in the literature [62, 72–76, 87, 92].

Sample, fabrication method	Avg. grain size	κ (W/m K)	σ (S/cm)	α (μV/K)	PF = $\sigma\alpha^2$ (μW/cmK^2)	ZT (300 K)	Ref.
$Bi_2Te_{2.7}Se_{0.3}$ nanocrystalline thin film, flash evaporation	60 nm	0.8 (cross-plane)	540	−186.1(in-plane)	18.7(in-plane)	0.7	[72]
Sintered bulk $Bi_2Te_{3-x}Se_x$ material, hot pressing	30 μm	1.6	930	−177.5	29.3	0.6	
Nanocrystalline bismuth-telluride-based ($Bi_2Te_{3-x}Se_x$) thin film	10 nm	0.61	550	−84.0	3.9	0.19	[73]
	27 nm	0.68	540	−138.1	10.3	0.46	
	60 nm	0.80	540	−186.1	18.7	0.70	
Nanocrystalline Bi-Sb-Te thin film, sputtering	26 nm	0.46	3.3	—	—	—	[75]
	45 nm	0.65	6.7	—	—	—	
	84 nm	0.81	33.3	—	—	—	
Nanocrystalline BiSbTe (8:30:62) thin film, flash evaporation	150 nm	0.6	—	—	—	—	[74]
Single crystal BiSbTe bulk alloys	—	0.75	—	—	—	—	[62]
Bi_2Te_3/Sb_2Te_3 superlattices (period ~5 nm)	—	0.4	—	—	—	—	[93]
$Bi_2Te_{3+0.63}$ bulk	—	2.2	1000	−240	58	0.87	[62]
$Bi_2(Te_{0.95}Se_{0.05})_3$ bulk	—	1.59	901	−223	45	0.85	[62]
$Bi_2Te_3/Bi_2(Te_{0.88}Se_{0.12})_3$ superlattice film, MBE	80 nm	1.25	639	−204	27	0.60	[87]
Bi_2Te_3 films, laser ablation	—	0.2–0.3	—	—	—	—	[92]
$Bi_xSb_{2-x}Te_3$ nanolayer film, PLD	190 nm	1.16	2700	95	25	0.65	[76]
$Bi_xSb_{2-x}Te_3$ nanodisk film, PLD	100 nm	1.00	1100	132	20	0.60	
$Bi_xSb_{2-x}Te_3$ nanocolumn film, PLD	70 nm	0.93	280	207	12	0.39	

Table 1. Room temperature thermal transport properties of nanocrystalline-nanostructured Bi_2Te_3-based thin films and bulk materials in the literature, including sample and fabrication method, average grain size, thermal conductivity κ, electrical conductivity σ, Seebeck coefficient α, power factor PF (= $\alpha^2\sigma$), and ZT (at 300 K).

Generally, the thermal conductivity κ value for polycrystalline films is expected to be smaller than that of bulk alloys because of the contribution of grain-boundary scattering [62, 72, 74]. Moreover, the κ of nanocrystalline Bi_2Te_3-based films will further decrease when the grain size of decreases (κ ≤ 0.81 W/mK) [73, 75]. For Bi_2Te_3/Sb_2Te_3 superlattice films, the coherent backscattering of phonon waves at the superlattice interfaces is outlined for the reduction of lattice thermal conductivity, resulting in the low κ ≤ 0.4 W/mK [93].

For PLD Bi_2Te_3-based films, Walachova et al. [92] estimated κ starting from direct ZT measurement with the Harman method and found a value of about 0.2–0.3 W/mK for films with a thickness comparable to our films (>100 nm). Recently, Chang et al. [76] reported the κ between 0.93 and 1.16 W/mK for granular $Bi_xSb_{2-x}Te_3$ films. The reported κ (at 300 K) of hexagonal flake Bi_2Se_3 was 0.75 W/mK.

6. Conclusion

We report the crystal, electronic structures, optical properties, and PEC activities of $BiVO_4$-based materials. Morphology engineering, cocatalyst loading, and doping with metal and nonmetal composite structures are the approaches to fabricate high efficiency $BiVO_4$ photoelectrode for PEC water spitting. In addition, the Bi_2Te_3-based thin films with nanocrystalline and nanostructured morphologies obtain the reduced thermal conductivity, meanwhile the close stoichiometric films with layered structure morphologies exhibit high thermoelectric power factors. $BiVO_4$-based materials and Bi_2Te_3-based thin films play significant roles for the photoelectrode and thermoelectric applications.

Acknowledgements

Financial support from Vietnam National Foundation for Science and Technology Development (NAFOSTED) under grant numbers 103.99–2015.17, 103.99-2016.75 (PHL), and MOST106-2119-M-009-011-MY3, Taiwan (CNV), is gratefully acknowledged.

Author details

Phuoc Huu Le[1]*, Nguyen Trung Kien[2] and Chien Nguyen Van[3,4]*

*Address all correspondence to: lhuuphuoc@ctump.edu.vn and chienft.u@gmail.com

1 Faculty of Basic Sciences, Can Tho University of Medicine and Pharmacy, Can Tho, Vietnam

2 Faculty of Medicine, Can Tho University of Medicine and Pharmacy, Can Tho, Vietnam

3 Department of Materials Science and Engineering, National Chiao Tung University, Hsinchu, Taiwan

4 Institute of Materials Science, Vietnam Academy of Science and Technology, Ha Noi City, Vietnam

References

[1] Li R, Han H, Zhang F, Wang D, Li C. Highly efficient photocatalysts constructed by rational assembly of dual-cocatalysts separately on different facets of $BiVO_4$. Energy & Environmental Science. 2014;**7**:1369. DOI: 10.1039/c3ee43304h

[2] Zhao X, Luo W, Feng J, Li M, Li Z, Yu T, Zou Z. Quantitative analysis and visualized evidence for high charge separation efficiency in a solid-liquid bulk heterojunction. Advanced Energy Materials. 2014;**4**:1301785. DOI: 10.1002/aenm.201301785

[3] Kim TW, Choi K-S. Nanoporous $BiVO_4$ photoanodes with dual-layer oxygen evolution catalysts for solar water splitting. Science. 2014;**343**:990-995. DOI: 10.1126/science.1246913

[4] Prévot MS, Sivula K. Photoelectrochemical tandem cells for solar water splitting. Journal of Physical Chemistry C. 2013;**117**:17879-17893. DOI: 10.1021/jp405291g

[5] Grätzel M. Photoelectrochemical cells. Nature. 2001;**414**:338-344. DOI: 10.1016/S0140-6736(06)68542-5

[6] Walter MG, Warren EL, James R. McKone JR, Boettcher SW, Mi Q, Santori EA, Lewis NS. Solar water splitting cells. Chemical Reviews. 2010;**110**:6446-6473. DOI: 10.1021/cr1002326

[7] Tan HL, Amal R. Alternative strategies in improving the photocatalytic and photoelectrochemical activities of visible light-driven $BiVO_4$: A review. Journal of Materials Chemistry A. 2017;**5**:16498-16521. DOI: 10.1039/C7TA04441K

[8] Xi G, Ye J. Synthesis of bismuth vanadate nanoplates with exposed {001} facets and enhanced visible-light photocatalytic properties. Chemical Communications. 2010; **46**:1893-1895. DOI: 10.1039/b923435g

[9] Li R, Han H, Zhang F, Wang D, Li C. Highly efficient photocatalysts constructed by rational assembly of dual-cocatalysts separately on different facets of $BiVO_4$. Energy & Environmental Science. 2014;**7**:1369. DOI: 10.1039/c3ee43304h

[10] Yu J, Kudo A. Effects of structural variation on the photocatalytic performance of hydrothermally synthesized $BiVO_4$. Advanced Functional Materials. 2006;**16**:2163-2169. DOI: 10.1002/adfm.200500799

[11] Huang Z-F, Pan L, Zou J-J, Zhang X, Wang L. Nanostructured bismuth vanadate-based materials for solar-energy-driven water oxidation: A review on recent progress. Nanoscale. 2014;(23):14044-14063. DOI: 10.1039/c4nr05245e

[12] Liang Y, Tsubota T, Mooij LPA, Krol R. Highly improved quantum efficiencies for thin film $BiVO_4$ photoanodes. Journal of Physical Chemistry C. 2011;**115**(35):17594-17598. DOI: 10.1021/jp203004v

[13] Tokunaga S, Kato H, Kudo A. Selective preparation of monoclinic and tetragonal $BiVO_4$ with Scheelite structure and their photocatalytic properties. Chemistry of Materials. 2001;**13**:4624-4628. DOI: 10.1021/cm0103390

[14] Kudo A, Omori K, Kato H. A novel aqueous process for preparation of crystal form-controlled and highly crystalline $BiVO_4$ powder from layered vanadates at room temperature and its photocatalytic and photophysical properties. Journal of the American Chemical Society. 1999;**121**:11459-11467. DOI: 10.1021/ja992541y

[15] Cooper JK, Gul S, Toma FM, Chen L, Glans PA, Guo J, Ager JW, Yano J, Sharp ID. Electronic structure of monoclinic $BiVO_4$. Chemistry of Materials. 2014;**26**(18):5365-5373. DOI: 10.1021/cm5025074

[16] Walsh A, Yan Y, Huda MN, Al-Jassim MM, Wei S-H. Band edge electronic structure of $BiVO_4$: Elucidating the role of the Bi s and V d orbitals. Chemistry of Materials. 2009;**21**(3):547-551. DOI: 10.1021/cm802894z

[17] Zhao Z, Li Z, Zou Z. Electronic structure and optical properties of monoclinic clinobisvanite $BiVO_4$. Physical Chemistry Chemical Physics. 2011;**13**:4746-4753. DOI: 10.1039/c0cp01871f

[18] Van CN, Chang WS, Chen J-W, Tsai K-A, Tzeng W-Y, Lin Y-C, Kuo H-H, Liu H-J, Chang K-D, Chou W-C, Wu C-L, Chen Y-C, Luo CW, Hsu Y-J, Chu Y-H. Heteroepitaxial approach to explore charge dynamics across Au/ $BiVO_4$ interface for photoactivity enhancement. Nano Energy. 2015;**15**:625-633. DOI: 10.1016/j.nanoen.2015.05.024

[19] Rettie AJE, Mozaffari S, Mcdaniel MD, Pearson KN, Ekerdt JG, Markert JT, Mullins CB. Pulsed laser deposition of epitaxial and polycrystalline bismuth vanadate thin films. Journal of Physical Chemistry C. 2014;**118**(46):26543-26550. DOI: 10.1021/jp5082824

[20] Stoughton S, Showak M, Mao Q, Koirala P, Hillsberry DA, Sallis S, Kourkoutis LF, Nguyen K, Piper LFJ, Tenne DA, Podraza NJ, Muller DA, Adamo C, Schlom DG. Adsorption-controlled growth of $BiVO_4$ by molecular-beam epitaxy. APL Materials. 2013;**1**:042112. DOI: 10.1063/1.4824041

[21] Luo W, Yang Z, Li Z, Zhang J, Liu J, Zhao Z, Wang Z, Yan S, Yu T, Zou Z. Solar hydrogen generation from seawater with a modified $BiVO_4$ photoanode. Energy & Environmental Science. 2011;**4**:4046-4051. DOI: 10.1039/c1ee01812d

[22] Sayama K, Nomura A, Arai T, Sugita T, Abe R, Yanagida M, Oi T, Iwasaki Y, Abe Y, Sugihara H. Photoelectrochemical decomposition of water into H_2 and O_2 on porous $BiVO_4$ thin-film electrodes under visible light and significant effect of Ag ion treatment. The Journal of Physical Chemistry. B. 2006;**3**:11352-11360. DOI: 10.1021/jp057539+

[23] Su J, Guo L, Bao N, Grimes CA. Nanostructured WO_3/$BiVO_4$ heterojunction films for efficient photoelectrochemical water splitting. Nano Letters. 2011;**11**:1928-1933. DOI: 10.1021/nl2000743

[24] Sui M, Han C, Wang Y, Li J, Gu X. Photoelectrochemical studies on $BiVO_4$ membranes deposition on transparent conductive substrates by a facile electrophoresis route. Journal of Materials Science: Materials in Electronics. 2016;**27**:4290-4296. DOI: 10.1007/s10854-016-4295-x

[25] Zhang Y, Guo Y, Duan H, Li H, Sun C, Liu H. Facile synthesis of $V4^{+}$ self-doped, [010] oriented $BiVO_4$ nanorods with highly efficient visible light- induced photocatalytic activity. Physical Chemistry Chemical Physics. 2014;**16**:24519-24526. DOI: 10.1039/C4CP03795B

[26] Neves MC, Trindade T. Chemical bath deposition of $BiVO_4$. Thin Solid Films. 2002;**406**:93-97. DOI: 10.1016/S0040-6090(01)01787-4

[27] Seabold JA, Choi K. Efficient and stable photo-oxidation of water by a bismuth vanadate photoanode coupled with an iron oxyhydroxide oxygen evolution catalyst. Journal of the American Chemical Society. 2012;**134**:2186-2192. DOI: 10.1021/ja209001d

[28] Song J, Cha J, Lee MG, Jeong HW, Seo S, Yoo JA, Kim TL, Lee J, No H, Kim DH, Jeong SY, An H, Lee BH, Bark CW, Park H, Jang HW, Lee S. Template-engineered epitaxial $BiVO_4$ photoanodes for efficient solar water splitting. Journal of Materials Chemistry A. 2017;**5**:18831-18838. DOI: 10.1039/C7TA04695B

[29] Van CN, Do TH, Chen J-W, Tzeng W-Y, Tsai K-A, Song H, Liu H-J, Lin Y-C, Chen Y-C, Wu C-L, Luo CW, Chou W-C, Huang R, Hsu Y-J, Chu Y-H. WO_3 mesocrystal-assisted photoelectrochemical activity of $BiVO_4$. NPG Asia Materials. 2017;**9**:e357. DOI: 10.1038/am.2017.15

[30] Kim JH, Lee JS. $BiVO_4$-based Heterostructured Photocatalysts for solar water splitting: A review. Energy and Environment Focus. 2014;**3**:339-353. DOI: 10.1166/eef.2014.1121

[31] Qiu Y, Liu W, Chen W, Chen W, Zhou G, Hsu P-C, Zhang R, Liang Z, Fan S, Zhang Y, Cui Y. Efficient solar-driven water splitting by nanocone $BiVO_4$-perovskite tandem cells. Science Advances. 2016;**2**:e1501764. DOI: 10.1126/sciadv.1501764

[32] Zhao J, Guo Y, Cai L, Li H, Wang KX, Cho IS, Lee CH, Fan S, Zheng X. High-performance ultrathin $BiVO_4$ photoanode on textured polydimethylsiloxane substrates for solar water splitting. ACS Energy Letters. 2016;**1**:68-75. DOI: 10.1021/acsenergylett.6b00032

[33] Kim TW, Choi K-S. Nanoporous BiVO4 photoanodes with dual-layer oxygen evolution catalysts for solar water splitting. Science. 2014;**343**:990-995. DOI: 10.1126/science.1246913

[34] Shi X, Choi IY, Zhang K, Kwon J, Kim DY, Lee JK, Oh SH, Kim JK, Park JH. Efficient photoelectrochemical hydrogen production from bismuth vanadate-decorated tungsten trioxide helix nanostructures. Nature Communications. 2014;**5**:4775. DOI: 10.1038/ncomms5775

[35] Park Y, McDonald KJ, Choi K-S. Progress in bismuth vanadate photoanodes for use in solar water oxidation. Chemical Society Reviews. 2013;**42**:2321-2337. DOI: 10.1039/c2cs35260e

[36] Rettie AJE, Lee HC, Marshall LG, Lin J-F, Capan C, Lindemuth J, McCloy JS, Zhou J, Bard AJ, Mullins CB. Combined charge carrier transport and photoelectrochemical characterization of $BiVO_4$ single crystals: Intrinsic behavior of a complex metal oxide. Journal of the American Chemical Society. 2013;**135**(30):11389-11396. DOI: 10.1021/ja405550k

[37] Li R, Zhang F, Wang D, Yang J, Li M, Zhu J, Zhou X, Han H, Li C. Spatial separation of photogenerated electrons and holes among {010} and {110} crystal facets of $BiVO_4$. Nature Communications. 2013;**4**:1432. DOI: 10.1038/ncomms2401

[38] Yang J, Wang D, Zhou X, Li C. A theoretical study on the mechanism of photocatalytic oxygen evolution on $BiVO_4$ in aqueous solution. Chemistry–A European Journal. 2013;(4):1320-1326. DOI: 10.1002/chem.201202365

[39] Li R, Han H, Zhang F, Wang D, Li C. Highly efficient photocatalysts constructed by rational assembly of dual-cocatalysts separately on different facets of $BiVO_4$. Energy & Environmental Science. 2014;**7**:1369-1376. DOI: 10.1039/c3ee43304h

[40] Tolod KR, Hernández S, Russo N. Recent advances in the $BiVO_4$ photocatalyst for sun-driven water oxidation: Top-performing photoanodes and scale-up challenges. Catalysts. 2017;**7**:13. DOI: 10.3390/catal7010013

[41] Li C, Zhang P, Lv R, Lu J, Wang T, Wang S, Wang H, Gong J. Selective deposition of Ag_3PO_4 on monoclinic $BiVO_4$(040) for highly efficient photocatalysis. Small. 2013;(23):3951-3956. DOI: 10.1002/smll.201301276

[42] Balachandran S, Prakash N, Thirumalai K, Muruganandham M, Sillanpa M, Swaminathan M. Facile construction of heterostructured $BiVO_4$–ZnO and its dual application of greater solar photocatalytic activity and self-cleaning property. Industrial and Engineering Chemistry Research. 2014;**53**:8346-8356. DOI: 10.1021/ie404287m

[43] Gao X, Wu HB, Zheng L, Zhong Y, Hu Y, Lou XWD. Formation of mesoporous heterostructured $BiVO_4/Bi_2S_3$ hollow discoids with enhanced photoactivity. Angewandte Chemie, International Edition. 2014;**53**:5917-5921. DOI: 10.1002/anie.201403611

[44] Grigioni I, Stamplecoskie KG, Selli E, Kamat PV. Dynamics of photogenerated charge carriers in $WO_3/BiVO_4$ heterojunction photoanodes. Journal of Physical Chemistry C. 2015;**119**:20792-20800. DOI: 10.1021/acs.jpcc.5b05128

[45] Rao PM, Cai L, Liu C, Cho IS, Lee CH, Weisse JM, Yang P, Zheng X. Simultaneously efficient light absorption and charge separation in $WO_3/BiVO_4$ core/shell nanowire photoanode for photoelectrochemical water oxidation. Nano Letters. 2014;**14**(2):1099-1105. DOI: 10.1021/nl500022z

[46] Hong SJ, Lee S, Jang JS, Lee JS. Heterojunction $BiVO_4/WO_3$ electrodes for enhanced photoactivity of water oxidation. Energy & Environmental Science. 2011;**4**:1781-1787. DOI: 10.1039/c0ee00743a

[47] Ma M, Kim JK, Zhang K, Shi X, Kim SJ, Moon JH, Park J. Double-deck inverse opal photoanodes: Efficient light absorption and charge separation in heterojunction. Chemistry of Materials. 2014;**26**:5592-5597. DOI: 10.1021/cm502073d

[48] Pihosh Y, Turkevych I, Mawatari K, Uemura J, Kazoe Y, Kosar S, Makita K, Sugaya T, Matsui T, Fujita D, Tosa M, Kondo M, Kitamori T. Photocatalytic generation of hydrogen

by core-shell WO_3/ $BiVO_4$ nanorods with ultimate water splitting efficiency. Scientific Reports. 2015;**5**:11141. DOI: 10.1038/srep11141

[49] Fu Y, Sun X, Wang X. $BiVO_4$–graphene catalyst and its high photocatalytic performance under visible light irradiation. Materials Chemistry and Physics. 2011;**131**:325-330. DOI: 10.1016/j.matchemphys.2011.09.049

[50] Ng YH, Iwase A, Kudo A, Amal R. Reducing graphene oxide on a visible-light $BiVO_4$ photocatalyst for an enhanced photoelectrochemical water splitting. Journal of Physical Chemistry Letters. 2010;**1**:2607-2612. DOI: 10.1021/jz100978u

[51] Wu X, Zhao J, Guo S, Wang L, Shi W, Huang H, Liu Y, Kang Z. Carbon dot and $BiVO_4$ quantum dot composites for overall water splitting via a two-electron pathway. Nanoscale. 2016;**8**:17314-17321. DOI: 10.1039/c6nr05864g

[52] Wang Y, Wang W, Mao H, Lu Y, Lu J, Huang J, Ye Z, Lu B. Electrostatic self-assembly of $BiVO_4$–reduced graphene oxide nanocomposites for highly efficient visible light photocatalytic activities. ACS Applied Materials & Interfaces. 2014;**6**:12698-12706. DOI: 10.1021/am502700p

[53] Zhao D, Zong W, Fan Z, Xiong S, Du M, Wu T, Fang Y-W, Ji F, Xu X. Synthesis of carbon-doped BiVO4@multi-walled carbon nanotubes with high visible-light absorption behavior, and evaluation of their photocatalytic properties. CrystEngComm. 2016;**18**:9007-9015. DOI: 10.1039/C6CE01642A

[54] Rao PM, Cai L, Liu C, Cho IS, Lee CH, Weisse JM, Yang P, Zheng X. Simultaneously efficient light absorption and charge separation in WO_3/$BiVO_4$ Core/Shell nanowire photoanode for photoelectrochemical water oxidation. Nano Letters. 2014;**14**(2):1099-1105. DOI: 10.1021/nl500022z

[55] Berglund SP, Rettie AJE, Hoang S, Mullins CB. Incorporation of Mo and W into nanostructured $BiVO_4$ films for efficient photoelectrochemical water oxidation. Physical Chemistry Chemical Physics. 2012;**14**:7065-7075. DOI: 10.1039/c2cp40807d

[56] Park HS, Kweon KE, Ye H, Paek E, Hwang GS, Bard AJ. Factors in the metal doping of $BiVO_4$ for improved photoelectrocatalytic activity as studied by scanning electrochemical microscopy and first-principles density-functional calculation. Journal of Physical Chemistry C. 2011;**115**:17870-17879. DOI: 10.1021/jp204492r

[57] Han L, Abdi FF, Krol RVD, Liu R, Huang Z, Lewerenz H-J, Dam B, Zeman M, Smets AHM. Efficient water-splitting device based on a bismuth vanadate photoanode and thin-film silicon solar cells. ChemSusChem. 2014;**7**:2832-2838. DOI: 10.1002/cssc.201402456

[58] Abdi FF, Han L, Smets AHM, Zeman M, Dam B, Krol RVD. Efficient solar water splitting by enhanced charge separation in a bismuth vanadate-silicon tandem photoelectrode. Nature Communications. 2013;**4**:2195. DOI: 10.1038/ncomms3195

[59] Venkatasubramanian R, Siivola E, Colpitts T, O'Quinn B. Thin-film thermoelectric devices with high room-temperature figures of merit. Nature. 2001;**413**:597-602. DOI: 10.1038/35098012

[60] Snyder GJ, Toberer ES. Complex thermoelectric materials. Nature Materials. 2008;**7**:105-114. DOI: 10.1038/nmat2090

[61] Dongfang Y, editor. Applications of Laser Ablation: Thin Film Deposition, Nanomaterial Synthesis and Surface Modification. Croatia: Intech; 2016. 55-84. doi: dx.doi.org/10.5772/65898

[62] Rowe DM, editor. Thermoelectrics Handbook: Macro to Nano. FL, Boca Raton: CRC/Taylor & Francis; 2006

[63] Nolas GS, Sharp J, Goldsmid HJ. Thermoelectrics: Basic Principles and New Materials Developments. New York: Springer; 2001

[64] Schumacher C, Reinsberg KG, Rostek R, Akinsinde L, Baessler S, Zastrow S, Rampelberg G, Woias P, Detavernier C, Broekaert JAC, Bachmann J, Nielsch K. Optimizations of pulsed plated p and n-type Bi_2Te_3-based ternary compounds by annealing in different ambient atmospheres. Advanced Energy Materials. 2013;**3**:95-104. DOI: 10.1002/aenm.201200417

[65] Soni A, Yanyuan Z, Ligen Y, Aik MKK, Dresselhaus MS. Enhanced thermoelectric properties of solution grown $Bi_2Te_{3-x}Se_x$ nanoplatelet composites. NanoLetters. 2012;**12**:1203-1209. DOI: 10.1021/nl2034859

[66] Le PH, Liao C-N, Luo CW, Lin J-Y, Leu J. Thermoelectric properties of bismuth-selenide films with controlled morphology and texture grown using pulsed laser deposition. Applied Surface Science. 2013;**285P**:657-663. DOI: 10.1016/j.apsusc.2013.08.107

[67] Le PH, Liao C-N, Luo CW, Lin J-Y, Leu J. Thermoelectric properties of nanostructured bismuth–telluride thin films grown using pulsed laser deposition. Journal of Alloys and Compounds. 2014;**615**:546-552. DOI: 10.1016/j.jallcom.2014.07.018

[68] Tuyen LTC, Le PH, Luo CW, Leu J. Thermoelectric properties of nanocrystalline Bi_3Se_2Te thin films grown using pulsed laser deposition. Journal of Alloys and Compounds. 2016;**673**:107-114. DOI: 10.1016/j.jallcom.2016.03.006

[69] Huang B, Lawrence C, Gross A, Hwang G-S, Ghafouri N, Lee S-W, Kim H, Li C-P, Uher C, Najafi K, Kaviany M. Low-temperature characterization and micropatterning of coevaporated Bi_2Te_3 and Sb_2Te_3 films. Journal of Applied Physics. 2008;**104**:113710. DOI: 10.1063/1.3033381

[70] Böttner H, Nurnus J, Gavrikov A, Kühner G, Jägle M, Künzel C, Eberhard D, Plescher G, Schubert A, Schlereth K-H. New thermoelectric components using microsystem technologies. International Journal of Energy & Environment. 2004;**13**:414-420. DOI: 10.1109/JMEMS.2004.828740

[71] Takashiri M, Shirakawa T, Miyazaki K, Tsukamoto H. Fabrication and characterization of bismuth-telluride-based alloy thin film thermoelectric generators by flash evaporation method. Sensors and Actuators A. 2007;**138**:329-334. DOI: 10.1016/j.sna.2007.05.030

[72] Takashiri M, Takiishi M, Tanaka S, Miyazaki K, Tsukamoto H. Thermoelectric properties of n-type nanocrystalline bismuth-telluride-based thin films deposited by flash evaporation. Journal of Applied Physics. 2007;**101**:74301. DOI: 10.1063/1.2717867

[73] Takashiri M, Miyazaki K, Tanaka S, Kurosaki J, Nagai D, Tsukamoto H. Effect of grain size on thermoelectric properties of n-type nanocrystalline bismuth-telluride based thin films. Journal of Applied Physics. 2008;**104**:84302. DOI: 10.1063/1.2990774

[74] Takashiri M, Tanaka S, Miyazaki K, Tsukamoto H. Cross-plane thermal conductivity of highly oriented nanocrystalline bismuth antimony telluride thin films. Journal of Alloys and Compounds. 2010;**490**:L44-L47. DOI: 10.1016/j.jallcom.2009.10.117

[75] Liao C-N, Wang Y-C, Chu H-S. Thermal transport properties of nanocrystalline Bi-Sb-Te thin films prepared by sputter deposition. Journal of Applied Physics. 2008;**104**:104312. DOI: 10.1063/1.3026728

[76] Chang H-C, Chen C-H, Kuo Y-K. Great enhancements in the thermoelectric power factor of BiSbTe nanostructured films with well-ordered interfaces. Nanoscale. 2013;**5**:7017-7025. DOI: 10.1039/c3nr01499a

[77] Chang H-C, Chen C-H. Self-assembled bismuth telluride films with well-aligned zero- to three-dimensional nanoblocks for thermoelectric applications. CrystEngComm. 2011;**13**:5956. DOI: 10.1039/c1ce05350g

[78] Noro H, Sato K, Kagechika H. The thermoelectric properties and crystallography of bi-Sb-Te-se thin films grown by ion beam sputtering. Journal of Applied Physics. 1993; **73**:1252-1260. DOI: 10.1063/1.353266

[79] Tritt TM. Thermoelectric phenomena, materials, and applications. Annual Review of Materials Research. 2011;**41**:433-448. DOI: 10.1146/annurev-matsci-062910-100453

[80] Li Bassi A, Bailini A, Casari CS, Donati F, Mantegazza A, Passoni M, Russo V, Bottani CE. Thermoelectric properties of Bi-Te films with controlled structure and morphology. Journal of Applied Physics. 2009;**105**:124307. DOI: 10.1063/1.3147870

[81] Chang H-C, Chen T-H, Whang W-T, Chen C-H. Superassembling of Bi_2Te_3 hierarchical nanostructures for enhanced thermoelectric performance. Journal of Materials Chemistry A. 2015;**3**:10459-10465. DOI: 10.1039/c5ta00911a

[82] Wang G, Endicott L, Uher C. Recent advances in the growth of Bi-Sb-Te-Se thin films. Science of Advanced Materials. 2011;**3**:539-560. DOI: 10.1166/sam.2011.1182

[83] https://www.lairdtech.com/

[84] Martin J, Wang L, Chen L, Nolas G. Enhanced seebeck coefficient through energy-barrier scattering in PbTe nanocomposites. Physical Review B. 2009;**79**:115311. DOI: 10.1103/PhysRevB.79.115311

[85] Deng Y, Liang H-M, Wang Y, Zhang Z-W, Tan M, Cui JL. Growth and transport properties of oriented bismuth telluride films. Journal of Alloys and Compounds. 2011;**509**:5683-5687. DOI: 10.1016/j.jallcom.2011.02.123

[86] Zhang Z, Wang Y, Deng Y, Xu Y. The effect of (00l) crystal plane orientation on the thermoelectric properties of Bi2Te3 thin film. Solid State Communications. 2011;**151**:1520-1523. DOI: 10.1016/j.ssc.2011.07.036

[87] Peranio N, Eibl O, Nurnus J. Structural and thermoelectric properties of epitaxially grown Bi_2Te_3 thin films and superlattices. Journal of Applied Physics. 2006;**100**:114306. DOI: 10.1063/1.2375016

[88] Zou H, Rowe DM, Min G. Growth of p- and n-type bismuth telluride thin films by co-evaporation. Journal of Crystal Growth. 2001;**222**:82-87. DOI: 10.1016/S0022-0248(00)00922-2

[89] Kadel K, Kumari L, Li WZ, Huang JY, Provencio PP. Synthesis and thermoelectric properties of Bi_2Se_3 nanostructures. Nanoscale Research Letters. 2010;**6**:57. DOI: 10.1007/s11671-010-9795-7

[90] Sun Z, Liufu S, Chen L. Synthesis and characterization of nanostructured bismuth selenide thin films. Dalton Transactions. 2010;**39**:10883-10887. DOI: 10.1039/c0dt00840k

[91] Al Bayaz A, Giani A, Artaud MC, Foucaran A, Delannoy FP, Boyer A. Growth parameters effect on the electric and thermoelectric characteristics of Bi_2Se_3 thin films grown by MOCVD. Journal of Crystal Growth. 2002;**241**:463-470. DOI: 10.1016/S0022-0248(03)01511-2

[92] Walachová J, Zeipl R, Zelinka J, Malina V, Pavelka M, Jelínek M, Studnička V, Lošťák P. High room-temperature figure of merit of thin layers prepared by laser ablation from Bi_2Te_3 target. Applied Physics Letters. 2005;**87**:081902. DOI: 10.1063/1.2001755

[93] Venkatasubramanian R. Lattice thermal conductivity reduction and phonon localization like behavior in superlattice structures. Physical Review B. 2000;**61**:3091-3097. DOI: 10.1103/PhysRevB.61.3091

IntechOpen